Substructuring based parametric reduced order modelling for large-scale dynamical systems containing viscoelasticity with application to bonded assemblies

Shuyang Zhang[1, 2], Hendrik Devriendt[1, 2], Lucas Van Belle[1, 2], Wim Desmet[1, 2]
[1] KU Leuven, Mechanical Engineering, LMSD division, Belgium
[2] Flanders Make, Core Lab DMMS, Belgium

Abstract:
Adhesive bonding plays an increasingly important role in mechanical systems to connect different components and multi-material assemblies, and usually exhibits viscoelasticity. To accurately predict their structural dynamic behavior, finite element models are often used. When large systems are considered, these models result in high computational costs. To reduce the computational costs, substructuring combined with model order reduction can be applied. In this context, the well-known Craig-Bampton method is often used. However, due to the frequency-dependency of viscoelastic material properties, it cannot be directly applied to assemblies with adhesive joints. To enable its use for viscoelastic substructures, this work proposes several improvements to the Craig-Bampton method. Moreover, since the dynamic performance of adhesive bonded structures can strongly depend on the viscoelastic properties, the efficient assessment of different material parameters is highly desirable. Therefore, this work also extends the improved Craig-Bampton method towards parametric model order reduction in which a global reduction basis is constructed by singular value decomposition and interpolation of sampling-based local bases. Two numerical examples of adhesive bonded systems are employed to demonstrate the accuracy and computation time reduction which can be achieved with the proposed approach.
Keywords: Improved Craig-Bampton method, local interface reduction, parametric model order reduction, substructuring, viscoelasticity

1 Introduction

Adhesive bonding is increasingly used to connect different components and multi-material assemblies, especially with the trend towards lightweight design. The behaviour of adhesive joints can significantly influence the structural dynamic properties of the assembly [1] due to the local changes in stiffness and damping they introduce. Many adhesive materials exhibit viscoelastic properties, which show both viscous and elastic characteristics when undergoing deformation and vibration, and typically strongly depend on frequency [2]. Several commonly used mathematical models have been proposed to describe the frequency-dependency in an explicit equation with frequency-independent parameters, such as the Golla-Hughes-McTavish model [3], generalized Maxwell model [4] and fractional derivative (FD) model [5]. This material property also exists in many other applications in mechanical systems, such as damping layers for vibration and noise suppression [6], [7]. To investigate the dynamic performance of large and complex mechanical systems with viscoelasticity, numerical models can be employed, with finite element (FE) models being used most often due to their high accuracy and direct link with physical parameters. Although simpler concept models exist [8], detailed FE models of joints are preferred to analyze the joint in detail, yet these can result in large model sizes and prohibitively long simulation times for real-life applications.

To improve the computational efficiency of high-fidelity FE models, a wide variety of model order reduction (MOR) techniques have been introduced which allow to significantly reduce the model size while maintaining good accuracy. Specifically, for the models with viscoelasticity, extensive research has been conducted to deal with their complex and frequency-dependent nature in order to allow MOR. Modal reduction methods, which rely on eigenmode computations, do typically no longer apply in presence of frequency-dependence. To overcome this, a polynomial approximation of the frequency-dependent model can be performed to still enable (complex) eigenmode computations, but this usually at least doubles the original model dimension for the modal computation, and leads to lower

computational efficiency and accuracy. Other strategies exist to extend modal reduction methods to handle frequency-dependent problems. For instance, the modal strain energy method [9], is a simple attempt to still use (un)damped linear modal information, but may result in an inaccurate reduced order model (ROM) for strong frequency-dependency. Several adaptations are proposed in [10] to improve the accuracy of this method by iteratively augmenting the reduction basis with modal information computed at several individual frequencies, thereby avoiding frequency-dependency in the eigenmode computation. In these approaches, the complex eigenproblem analysis has to be conducted several times, which could be time-consuming. Another way to deal with frequency-dependency is to introduce extra dissipative coordinates [11] and then apply modal methods, but this inevitably increases the model size and is only applicable for specific viscoelastic models.

As an alternative to modal method extensions, the Krylov subspace based reduction method has also been proposed for models including frequency-dependency [12]. Before applying this method, the frequency-dependent model needs to be transformed into polynomial terms. By using a polynomial expansion, which is applicable to all types of viscoelastic models, the frequency-dependency can be implicitly embedded into the second-order dynamic system equations. When a fractional order model (such as the FD model) is employed, alternative methods exist for approximation by fractional operators [13], [14], especially for the non-integer order term of the viscoelastic model. However, these methods first construct the rational approximation, and then form the state-space representation of the original model leading to augmented state vectors, which inevitably increases the dimension of the model, or still needs the polynomial approximation. Therefore, it could be more efficient to directly use the polynomial approximation. Other methods like AAA approximation [15] represent the data-based method, which does not fully take the advantage of model-based reduction methods. Thus, the polynomial approximation stands out. After representing the model into second order polynomials, a reduction basis from the second-order Krylov subspace is generated by the second-order Arnoldi (SOAR) algorithm [16]. Similarly, the higher-order Krylov subspace [17] is also found employed [18], [19]. Moreover, the iterative rational Krylov algorithm [20] is also extended to the frequency-dependent problem [21].

Different parameters of viscoelasticity could result in significantly different dynamic properties of the system. When the change of these parameters in the model needs to be investigated, such as in the design phase, in the process of model-based parameter identification, or even in uncertainty quantification, reduced-order models (ROMs) are usually incompatible with parameter changes: a ROM generated for a given set of parameters cannot accurately approximate the full order model (FOM) with another set of parameters. Therefore, parametric model order reduction (pMOR) [22], [23] is proposed to enable one reduced model to accurately approximate the FOM within a range of parameters. pMOR techniques can in general be divided into two types based on whether or not sampling is needed. Unsampled pMOR techniques [24], [25] usually have the advantage of resulting in ROMs with a relatively small dimension in fewer steps, but also have the strong limitation that only low-rank changes in the system can occur. For frequency-dependent substructures, this method may not be applicable since the frequency-dependent part may take up a large portion of the joint substructure. Instead, in this work, pMOR with sampling will be used to construct parametric ROMs for adhesive joint substructures. The sampling methods can also be clustered into two types: uniform/(quasi-)random sampling and sampling based on model information [26]–[28]. Although the second type could be more accurate, the sampling process can be cumbersome and might result in a large number of samples. After generating samples with a suitable (quasi-)random sampling approach, the local reduction bases are computed at these samples and they can be collected column-wise to form the global reduction basis [22]. Another way to generate a global reduction basis is to interpolates the bases from the adjacent samples [29].

pMOR provides an efficient way for the model simulation, while the reduction process might be gradually time-consuming with the increased dimension. To make it more efficient for large-scale FE models, substructuring [30], [31] can be employed and combined with pMOR. This technique divides the whole FE model into several smaller substructures, which can be processed separately. The benefits are apparent: it offers the flexibility of considering local parameters and local dynamic behavior only in the specific joint substructures, and reduction of a substructure with local properties is simpler and faster than of the entire model. Component modal analysis (CMS) is a well-known group of modal reduction methods that combines MOR with substructuring. In these methods, the degrees of freedom (DOFs) of a substructure are usually divided into the interface DOFs, which connect to the other

substructures, and the remaining, internal DOFs. The commonly used Craig-Bampton (CB) method [32] considers each substructure with a fixed interface and uses the superposition of static constraint interface modes and interior normal modes to represent the deformation of the internal DOFs. The reduction is achieved by truncation of these interior normal modes. Other CMS methods exist as well which consider a free interface, such as the MacNeal [33] and Rubin method [34]. Although these CMS methods successfully reduce the internal DOFs of substructures, the amount of interface DOFs remains unchanged. This can be dealt with using interface reduction (IR), for which several methods have been developed [35]–[37]. The characteristic constraint mode (CCM) method [38] for instance reduces the remaining interface DOFs of the assembled substructures with a truncated set of interface normal modes. Although this method can achieve relatively high accuracy, it requires information from the interfaces of the entire system assembly. Instead, local interface reduction (LIR) only uses the information from the substructure itself to reduce its interface while not being influenced by other substructures. The local characteristic constraint mode (LCCM) method [39] is the LIR counterpart of the CCM. The method has the same rationale, but only applies to the interface of the individual substructure. After LCCM is applied to the substructures, the local reduction bases of the interfaces from neighboring substructures need to be compatible for assembly, for which several approaches are summarized in [40].

In both CMS and LIR, modes are used to generate reduction bases for the substructures. However, the modes used in these methods usually are only computed from linear elastic systems. In [41], [42], the second-order Krylov subspace in combination with the CB method was also proposed, but only for linear elastic structures with constant properties. When frequency-dependency of viscoelasticity occurs in the assembly, these methods can hardly be directly applied. Therefore, although many effective MOR methods are developed for viscoelastic systems, the gap between the MOR of systems with viscoelasticity and substructuring still exists. Consequently, there is also no direct pMOR approach in context of substructuring for large-scale mechanical systems with viscoelasticity.

Therefore, the goal of this paper is to propose a pMOR approach in context of substructuring for the efficient analysis of large-scale assemblies containing viscoelasticity. To achieve this goal, four improvements to the state-of-the-art are proposed. The first three aim to enable the use of the CB method as the basic technique for the reduction of viscoelastic substructures and correspond to the three different parts of the CB reduction basis: i) the reduction basis for the interior: using Taylor expansion [12] to implicitly embed the frequency-dependency into the equations of motion and using the second-order Krylov subspace to construct the reduction basis instead of the normal modes; ii) the constraint modes: the frequency-dependency is circumvented by re-expressing the constraint modes after expansion and re-representing of the original model; iii) the reduction basis for the interface: the basis vectors of the Krylov subspace are used in the LCCM instead of interface normal modes. The fourth improvement iv) aims to enable the construction of a global reduction basis based on the improvements i)-iii) above combined with primal assembly to form the pROM of the entire jointed structure.

The rest of this paper is organized as follows. In Section 2, the workflow of the general methodology is briefly explained. In Section 3, the viscoelastic behavior and the relative mathematical model are introduced, and the FE model of a structure with viscoelastic components is briefly formulated. In Section 4, the basic theory of the reduction techniques involved in the methodology are introduced. Improvements i)-iii) proposed for the CB method and LCCM, as well as iv) for the pMOR method, are discussed in detail in Sections 5 and 6, respectively. The methodology is implemented and applied to two numerical examples for the frequency-domain analysis in Section 7: a simple single lap adhesive joint model and a more complex wing flap model. The main conclusions are summarized in Section 8.

2 General methodology

The proposed methodology to enable substructuring with pMOR for fast frequency-domain analysis of systems containing viscoelasticity, includes three main steps (Figure 1): generating substructures according to the material configuration, applying pMOR to reduce these substructures, and reassembling the substructures. After repeating the main aspects of viscoelastic material modelling in a finite element context in Section 3, the basic techniques in these three steps are briefly introduced in Section 4 and the improvements proposed in this work are explained in detail in Section 5 and 6.

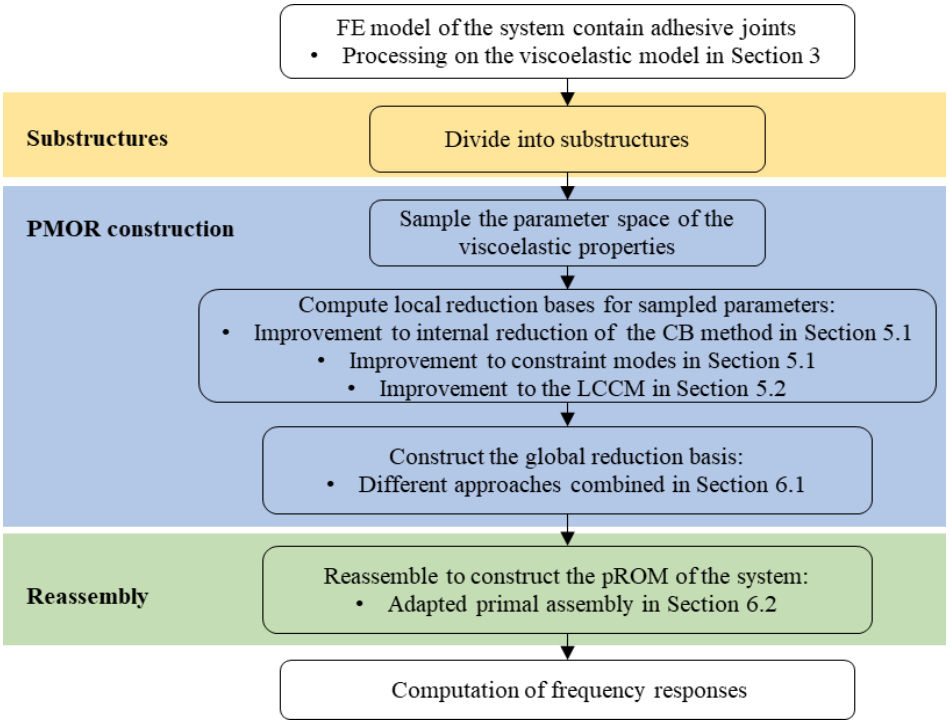

Figure 1: Flowchart of the general methodology.

3 Modelling of mechanical systems with viscoelastic adhesive joints

To build the FE model of a mechanical system containing viscoelastic adhesive joints, an appropriate mathematical model is needed to numerically represent the frequency-dependency of the viscoelastic behavior. In this section, the definition and the used numerical model of the viscoelastic behavior are first introduced. Then, the FE model of a structure containing a viscoelastic joint is briefly formulated.

3.1 Viscoelastic behavior

The frequency-dependency of viscoelastic materials can be defined by the complex shear modulus, which in frequency domain is expressed as:

$$G(\omega) = G_s(\omega) + jG_l(\omega), \tag{1}$$

in which G_s and G_l respectively represent the storage modulus and the loss modulus, $\omega = 2\pi f$ is the angular frequency with frequency f, and $j^2 = -1$. The ratio of two moduli G_l/G_s is defined as the loss factor, representing the dissipation property of viscoelastic materials.

To describe the frequency-dependency of Eq. (1) in an explicit equation with frequency-independent parameters, the FD model is employed in this work since it is well-suited for predicting the dynamic behavior over a wide frequency range [12]. It contains four coefficients and is defined in function of the Laplace variable $s=j\omega$ as:

$$G(s) = (G_0+G_\infty(s\tau)^\alpha)/(1+(s\tau)^\alpha), \tag{2}$$

where G_0 and G_∞ represent the dynamic modulus at zero frequency and the high-frequency value of the dynamic modulus, τ is the relaxation time and α is the fractional-order time derivative located in the closed interval [0, 1]. These four coefficients govern the viscoelastic behavior and are considered as the parameters for the construction of the pROM in Section 6.

3.2 Finite element model of a structure containing viscoelastic materials

With the viscoelastic behavior well-defined, an FE model of a structure containing viscoelasticity can be constructed. The stress-strain relationship of the viscoelastic material in the Laplace domain for small deformations can be expressed as

$$\boldsymbol{\sigma}(s) = \boldsymbol{c}(s)\boldsymbol{\varepsilon}(s), \tag{3}$$

with stress $\boldsymbol{\sigma}$ and strain $\boldsymbol{\varepsilon}$, and where $\boldsymbol{c}(s)$ is the viscoelasticity matrix, which contains the complex dynamic modulus $G(s)$ defined by the FD model. Extracting $G(s)$ from $\boldsymbol{c}$(s) results in the following format with affine parameter dependency [43]:

$$\boldsymbol{c}(s) = G(s)\boldsymbol{c}_0. \tag{4}$$

In this expression, $\boldsymbol{c}_0$ is a constant matrix and the frequency-dependency is only contained within $G(s)$. Upon FE discretization of the linear elastic structure containing a viscoelastic joint [44], the stiffness matrix $\boldsymbol{K}_{ve}$ related to the viscoelastic material part of the structure is represented as

$$\boldsymbol{K}_{ve} = \bigcup \boldsymbol{k}_v = \bigcup G(s) \int \boldsymbol{\varepsilon}^{\mathrm{T}} \boldsymbol{c}_0^{\mathrm{T}} \boldsymbol{\varepsilon} \, \mathrm{d}V = G(s)\boldsymbol{K}_v, \tag{5}$$

where $\boldsymbol{k}_v$ is the stiffness matrix of each single element in the viscoelastic part and the symbol $\cup$ denotes the assembly of element matrices. $\boldsymbol{K}_v$ is the basic stiffness matrix after extracting $G(s)$ out of the complex stiffness matrix, which is constant. Having access to $G(s)$ as an affine parameter will be beneficial for the pMOR since it provides direct access to local parameters. By also introducing the structure's mass matrix $\boldsymbol{M}$ and the stiffness matrix of the elastic part $\boldsymbol{K}_e$ of the structure, the structural dynamic FE model of the structure containing a viscoelastic joint is represented as:

$$(s^2\boldsymbol{M} + G(s)\boldsymbol{K}_v + \boldsymbol{K}_e)\boldsymbol{q} = \boldsymbol{F}, \tag{6}$$

where $\boldsymbol{F}$ is the external load vector and $\boldsymbol{q}$ is the displacement vector. Since the proposed method is tailored to deal with viscoelasticity, for clarity only damping originating from viscoelasticity is considered in this work. However, without loss of generality, the method can also be applied when viscous and structural damping are present.

4 Basics of substructuring and the CB method

Before explaining the improvements proposed in this work, the basic theories of substructuring and the CB method for reduction are briefly introduced in Section 4.1 and 4.2, respectively.

4.1 Substructures and reassembly

As modelled with Eq. (6), a large-scale system with adhesive joints as the viscoelastic part can be decomposed into substructures including the parts of joint regions. This is illustrated in Fig. 2 for a single lap joint, where this procedure results in a joint substructure which contains the viscoelastic adhesive material and part of the joined substrates, and two other substructures containing only linear elastic materials of the substrates. The resulting equations of motion of the substructures can in general be expressed as:

$$(s^2\boldsymbol{M}^{(l)} + G(s)\boldsymbol{K}_v^{(l)} + \boldsymbol{K}_e^{(l)})\,\boldsymbol{q}^{(l)} = \boldsymbol{F}^{(l)} + \boldsymbol{g}^{(l)}, \tag{7}$$

The vector $\boldsymbol{g}$ represents the internal connecting forces, which are located at the interface with the adjacent substructures. The superscript l indicates the numbering of the substructure, and is omitted in the rest of the paper unless specifically mentioned otherwise, for the sake of simplicity. By decomposing the adhesive joint region(s) into separate substructure(s), the viscoelastic part $G(s)\boldsymbol{K}_v^{(l)}$ will only be nonzero in the adhesive joint substructure(s).

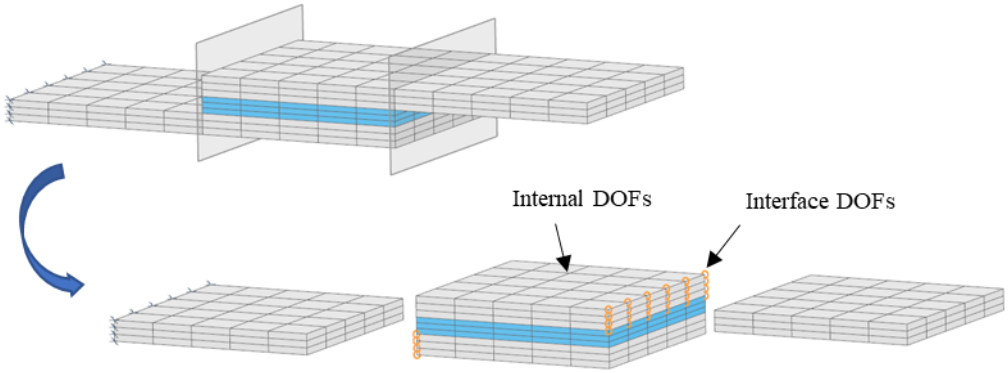

Figure 2: Schematic of dividing substructures.

For the assembly of substructures, with or without applying model reduction to the substructures, information from the interface between adjacent substructures is needed. This information can be the compatibility conditions (primal assembly) or the equilibrium conditions (dual assembly) of the FE model. Since dual assembly enlarges the dimension of the original FE model, in this work, the primal assembly is employed. This approach uses a Boolean matrix $\boldsymbol{L}$ to represent the relationship between the DOFs $\boldsymbol{q}$ of the assembled FE model and the concatenated DOFs $\boldsymbol{u}$ of all the disconnected substructures:

$$\boldsymbol{u} = \boldsymbol{L}\boldsymbol{q}. \tag{8}$$

Since the internal connection forces at the same interface for two adjacent substructures must be the same magnitude while opposite direction, and according to the definition of the Boolean matrix $\boldsymbol{L}$, the relation between the internal connecting forces $\boldsymbol{g}$ can be expressed as

$$\boldsymbol{L}^{\mathrm{T}}\boldsymbol{g} = \boldsymbol{0}. \tag{9}$$

Similarly to $\boldsymbol{u}$, vector $\boldsymbol{g}$ is the collection of $\boldsymbol{g}^{(l)}$. With this equation, the unknown internal forces $\boldsymbol{g}$ can be eliminated after reassembly of the substructures. For reassembly of the reduced substructures, the compatibility conditions defined by the physical DOFs in Eq. (8) are constructed from the reduced substructures, which is introduced in Section 6.2.

4.2 The CB method

The CB method is one of the most popular and accurate reduction techniques in context of substructuring in industry and academia [40]. This method first divides the model of the substructure, as shown in Eq. (7), into the internal and interface DOFs, which can be expressed as:

$$\left(s^2\begin{bmatrix}\boldsymbol{M}_{ii} & \boldsymbol{M}_{ib}\\ \boldsymbol{M}_{bi} & \boldsymbol{M}_{bb}\end{bmatrix} + G(s)\begin{bmatrix}\boldsymbol{K}_{v,ii} & \boldsymbol{K}_{v,ib}\\ \boldsymbol{K}_{v,bi} & \boldsymbol{K}_{v,bb}\end{bmatrix} + \begin{bmatrix}\boldsymbol{K}_{e,ii} & \boldsymbol{K}_{e,ib}\\ \boldsymbol{K}_{e,bi} & \boldsymbol{K}_{e,bb}\end{bmatrix}\right)\begin{bmatrix}\boldsymbol{q}_i\\ \boldsymbol{q}_b\end{bmatrix} = \begin{bmatrix}\boldsymbol{F}_i\\ \boldsymbol{0}\end{bmatrix} + \begin{bmatrix}\boldsymbol{0}\\ \boldsymbol{g}_b\end{bmatrix}. \tag{10}$$

Subscripts i and b indicate the internal partition and interface (Figure 2), while subscripts ib and bi indicate the coupling parts. Then the reduction basis $\boldsymbol{V}_{\mathrm{CB}}$ of the standard CB method is defined as

$$\boldsymbol{V}_{\mathrm{CB}} = \begin{bmatrix}\boldsymbol{\phi} & \boldsymbol{\psi}\\ \boldsymbol{0} & \boldsymbol{I}\end{bmatrix}. \tag{11}$$

Herein, $\boldsymbol{I}$ is an identity matrix. $\boldsymbol{\phi}$ represents the set of truncated interior normal modes, that achieves the reduction of the internal DOFs. In absence of viscoelasticity, these interior normal modes are computed from the eigenproblem of the internal partition. $\boldsymbol{\psi}$ is the set of static constraint modes, computed as

$$\boldsymbol{\psi} = -\boldsymbol{K}_{ii}^{-1}\boldsymbol{K}_{ib}. \tag{12}$$

To further improve computational efficiency, LCCM is employed to reduce the remaining interface DOFs after applying the CB method, by a second eigenproblem analysis:

$$\left(\lambda^2\widehat{\boldsymbol{M}}_{bb} + \widehat{\boldsymbol{K}}_{bb}\right)\boldsymbol{\phi}_{bb} = \boldsymbol{0}, \tag{13}$$

where $\widehat{\boldsymbol{M}}_{bb}$ and $\widehat{\boldsymbol{K}}_{bb}$ are the mass and stiffness matrices of the interface after applying the CB method.

5 Improvements on CB method with LCCM for viscoelasticity

Since the CB method and LCCM cannot be directly applied to the frequency-dependent viscoelastic substructures of interest, as the prerequisite modes cannot be directly computed, this section proposes three improvements to make this method applicable. In what follows, Section 5.1 introduces two improvements to the CB method, and Section 5.2 introduces the improvement to the LCCM.

5.1 Improvements on the CB method

Considering a frequency-dependent stiffness matrix, as is the case for viscoelasticity, it is clear that the constant $\boldsymbol{\phi}$ or $\boldsymbol{\psi}$ in Eq. (11) cannot be generated according to their definitions. Therefore, new approaches for constructing these two components of the reduction basis are proposed.

5.1.1 Krylov subspace for the internal reduction

The modal reduction of the internal part in the CB method is processed independently due to the use of constraint modes, as shown in Eq. (11). Inspired by this, the equations of motion used in the reduction for the internal partition of the joint substructure can be simplified without considering the coupling terms in the first line of Eq. (10), and are expressed as

$$(s^2\boldsymbol{M}_{ii} + G(s)\boldsymbol{K}_{v,ii} + \boldsymbol{K}_{e,ii})\boldsymbol{q}_i = \boldsymbol{F}_i + \boldsymbol{g}_i. \tag{14}$$

To make Eq. (14) suitable for MOR methods which rely on second-order system equations, a Taylor series expansion of the high-order differentiable rational function in the FD model is employed. The scalar function $G(s)$ in the frequency-dependent part is expanded as

$$G(s) = G(s_0) + G^{'}(s_0)(s\text{-}s_0) + G^{''}(s_0)(s\text{-}s_0)^2/2 + R_2(s), \tag{15}$$

where $G^{'}$ and $G^{''}$ represent the first two orders of derivatives. s_0 is a given expansion point and can be any value of interest in the Laplace domain. This way, the frequency-dependency is transferred to a second-order form with a higher-order residual and $\lim_{s\to s_0} R_2(s)=0$ [12]. Substituting Eq. (15) into Eq. (14), and introducing the expansion point for the model, the equations of motion for the internal partition can be re-expressed in second-order format as

$$((s\text{-}s_0)^2\widetilde{\boldsymbol{M}}_{ii} + (s\text{-}s_0)\widetilde{\boldsymbol{C}}_{ii} + \widetilde{\boldsymbol{K}}_{ii} + R_2(s)\boldsymbol{K}_{v,ii})\boldsymbol{q}_i = \boldsymbol{F}_i + \boldsymbol{g}_i, \tag{16}$$

where

$$\widetilde{\boldsymbol{M}}_{ii} = \boldsymbol{M}_{ii} + G^{''}\boldsymbol{K}_{v,ii}/2,\ \ \widetilde{\boldsymbol{C}}_{ii} = 2s_0\boldsymbol{M}_{ii} + G^{'}\boldsymbol{K}_{v,ii},\ \ \widetilde{\boldsymbol{K}}_{ii} = s_0^2\boldsymbol{M}_{ii} + G\boldsymbol{K}_{v,ii} + \boldsymbol{K}_{e,ii}. \tag{17}$$

Since the vector $\boldsymbol{g}$ only contains non-zero values for the interface DOFs, and the external load $\boldsymbol{F}$ is considered to be applied at other substructures, the right side of the equations can be zero. This allows rewriting Eq. (16) as follows:

$$((s\text{-}s_0)^2\widetilde{\boldsymbol{M}}_{ii} + (s\text{-}s_0)\widetilde{\boldsymbol{C}}_{ii} + \widetilde{\boldsymbol{K}}_{ii} + R_2(s)\boldsymbol{K}_{v,ii})\boldsymbol{q}_i = \boldsymbol{B}_{\mathrm{u}}u, \tag{18}$$

where $\boldsymbol{B}_{\mathrm{u}}$ represents the input vector, which is a unity vector, and the input u is zero. In case any external load $\boldsymbol{F}_i$ is applied on the joint substructure, this equation can be easily adapted by replacing $\boldsymbol{B}_{\mathrm{u}}$ to an input matrix, that each column indicates the location of a unique input. With the new expression in Eq. (18), the frequency-dependency is implicitly embedded into the substructure model, but all the system matrices are constant. If viscous and/or structural damping would be considered, these can simply be added into $\widetilde{\boldsymbol{C}}_{ii}$ and $\widetilde{\boldsymbol{K}}_{ii}$. As mentioned in Section 3.2, the method can be readily applied without loss of generality to such cases, but for clarity only viscoelasticity is further considered.

Then, the point s_0 in Eq. (18) can be associated with the expansion point in the Krylov subspace based reduction method, and the second-order Krylov subspace method can be employed to generate a constant reduction basis for this frequency-dependent model. Although several works have proposed adaptive expansion point selection methods [24], only a single expansion point is selected here, which can be combined with a higher order at this expansion point to increase accuracy. An orthonormal vector sequence $\{\boldsymbol{r}_0, \boldsymbol{r}_1, \ldots, \boldsymbol{r}_{\mathrm{n}}\}$ that spans the Krylov subspace forms the reduction basis $\boldsymbol{V}_i \in \boldsymbol{R}^{N_i \times n_i}$ for the internal partition of the joint substructure. N_i indicates the full dimension of the original model, and n_i indicates the reduced dimension which is also called the order of the reduction basis from the Krylov subspace. These vectors are computed by the second-order Arnoldi Algorithm [16] and have iterative relations as

$$\begin{cases} \boldsymbol{r}_1 = \boldsymbol{P}\boldsymbol{r}_0 \\ \boldsymbol{r}_l = \boldsymbol{P}\boldsymbol{r}_{l\text{-}1} + \boldsymbol{Q}\boldsymbol{r}_{l\text{-}2},\ \ l \geq 2 \end{cases}, \tag{19}$$

where

$$\boldsymbol{P} = \text{-}\widetilde{\boldsymbol{K}}_{ii}^{\ \text{-}1}\widetilde{\boldsymbol{C}}_{ii},\ \ \boldsymbol{Q} = \text{-}\widetilde{\boldsymbol{K}}_{ii}^{\ \text{-}1}\widetilde{\boldsymbol{M}}_{ii},\ \ \boldsymbol{r}_0 = \text{-}\widetilde{\boldsymbol{K}}_{ii}^{\ \text{-}1}\boldsymbol{B}_{\mathrm{u}}. \tag{20}$$

Projecting the system matrices of Eq. (14) onto the subspace spanned by the reduction basis $\boldsymbol{V}_i$, the reduced model of the internal partition is generated as

$$((s\text{-}s_0)^2\widetilde{\boldsymbol{M}}_{ii,r} + (s\text{-}s_0)\widetilde{\boldsymbol{C}}_{ii,r} + \widetilde{\boldsymbol{K}}_{ii,r} + R_2(s)\boldsymbol{K}_{vii,r})\boldsymbol{q}_{i,r} = \boldsymbol{B}_{\mathrm{u},r}u. \tag{21}$$

The subscript r denotes the reduced counterparts of the full-order matrices and vectors. Then, by combining the additional terms after expansion to their original matrices, the reduced model of the internal partition of the joint substructure in Eq. (21) can be retrieved as

$$(s^2\boldsymbol{M}_{ii,r} + G(s)\boldsymbol{K}_{vii,r} + \boldsymbol{K}_{eii,r})\boldsymbol{q}_{i,r} = \boldsymbol{B}_{\mathrm{u},r}u. \tag{22}$$

The reduced matrices and vectors in this reduced model are expressed as

$$\boldsymbol{M}_{ii,r} = \boldsymbol{V}_i^{\mathrm{T}}\boldsymbol{M}_{ii}\boldsymbol{V}_i,\ \ \boldsymbol{K}_{vii,r} = \boldsymbol{V}_i^{\mathrm{T}}\boldsymbol{K}_{v,ii}\boldsymbol{V}_i,\ \ \boldsymbol{K}_{eii,r} = \boldsymbol{V}_i^{\mathrm{T}}\boldsymbol{K}_{e,ii}\boldsymbol{V}_i,\ \ \boldsymbol{B}_{\mathrm{u},r} = \boldsymbol{V}_i^{\mathrm{T}}\boldsymbol{B}_{\mathrm{u}}. \tag{23}$$

5.1.2 New expression of the constraint modes for viscoelasticity

Also in the computation of constraint modes $\boldsymbol{\psi}_f$, frequency-dependent terms are involved according to the definition in Eq. (12). To circumvent this, $\boldsymbol{\psi}_f$ can be re-expressed based on the reformulated

system of equations of Eq. (18), whereby the $\boldsymbol{K}_{ii}$ used in Eq. (12) can be replaced by the $\widetilde{\boldsymbol{K}}_{ii}$ of Eq. (17). This allows expressing the constant constraint modes $\boldsymbol{\psi}_f$ of this frequency-dependent viscoelastic substructure as

$$\boldsymbol{\psi}_f = -(s_0^2\boldsymbol{M}_{ii} + G\boldsymbol{K}_{v,ii} + \boldsymbol{K}_{e,ii})^{-1}(s_0^2\boldsymbol{M}_{ib} + G\boldsymbol{K}_{v,ib} + \boldsymbol{K}_{e,ib}). \tag{24}$$

In this equation, s_0 still represents the expansion point. As before, one expansion point is employed. It should be noted that this expansion point does not have to be the same as for the internal reduction.

With these two improvements to the CB method, the reduction basis is now applicable to frequency-dependent viscoelastic substructures, while still preserving its original structure expressed as

$$\boldsymbol{V}_f = \begin{bmatrix} \boldsymbol{V}_i & \boldsymbol{\psi}_f \\ \boldsymbol{0} & \boldsymbol{I} \end{bmatrix}. \tag{25}$$

5.2 Krylov based LCCM

Classical LCCM relies on a normal mode computation to reduce the interface. However, since a frequency-dependent interface is considered in the case of viscoelastic substructures, the LCCM has the same issue as the interior reduction in the CB method since constant normal modes cannot be computed. Therefore, the second order Krylov subspace method is again employed instead to form a new LCCM reduction basis $\boldsymbol{V}_b$, based on the second order equations of the interface:

$$\left(s^2\widehat{\boldsymbol{M}}_{bb} + G(s)\widehat{\boldsymbol{K}}_{v,bb} + \widehat{\boldsymbol{K}}_{e,bb}\right)\boldsymbol{q}_b = \boldsymbol{B}_{\mathrm{u}}u. \tag{26}$$

Then, $\boldsymbol{V}_{\mathrm{b}}$ is computed through a similar process as described for the interior reduction in Section 5.1.1. One expansion point is again selected for generating this reduction basis, and the value of this expansion point can also be different from the expansion points for the internal partition and the constraint modes. Combined with the improved CB method of Section 5.1, the new reduction basis $\boldsymbol{V}_{\mathrm{a}}$ for the reduction of the complete, frequency-dependent viscoelastic substructure is finally represented as

$$\boldsymbol{V}_{\mathrm{a}} = \boldsymbol{V}_f\begin{bmatrix} \boldsymbol{I} & \boldsymbol{0} \\ \boldsymbol{0} & \boldsymbol{V}_{\mathrm{b}} \end{bmatrix} = \begin{bmatrix} \boldsymbol{V}_i & \boldsymbol{\psi}_f\boldsymbol{V}_{\mathrm{b}} \\ \boldsymbol{0} & \boldsymbol{V}_{\mathrm{b}} \end{bmatrix}. \tag{27}$$

6 Parametric model order reduction based on the improved CB method with LCCM

In this section, the improved CB method with LCCM is extended to pMOR, to leverage the advantages of substructuring for local change of parameters in dynamic analysis and to make the ROM compatible with parameter changes.

The four coefficients of the FD model for the viscoelastic material are the targeted parameters for pROM construction of the viscoelastic substructures in this work, and the pMOR strategy employed relies on a sampling-based construction of a global reduction basis. This approach consists of three steps: (i) sampling of the parameter space, (ii) generating local reduction bases, and (iii) constructing the global reduction basis.

The sampling technique employed in this work is quasi-random sampling, which selects samples that are well-distributed in the entire parameter space. This type of sampling is predetermined and not dependent on the output of the model, which could benefit the efficiency of the sampling process. The local reduction basis is computed by the improved CB method with LCCM. Since the three compositions of this reduction basis are generated in different ways, the construction of these compositions in the global reduction basis can be also different and discussed in detail in Section 6.1. This global reduction basis is also used to build the assembly relations between substructures, leading to the pROM of the complete system containing viscoelastic materials, which is introduced in Section 6.2.

6.1 Construction of the global reduction basis

Local reduction bases computed by the improved CB method with LCCM are used to generate the global reduction basis. Since the corresponding $\boldsymbol{V}_i$, $\boldsymbol{\psi}_f$ and $\boldsymbol{V}_b$ are computed using different concepts, different approaches are applied to construct the corresponding global reduction basis components.

6.1.1 Global reduction basis for $\boldsymbol{V}_i$ and $\boldsymbol{V}_b$

The global reduction basis $\boldsymbol{V}_{ip}$ for the internal partition is obtained by concatenating the local reduction bases:

$$\boldsymbol{V}_{ip} = [\boldsymbol{V}_{i,1} \quad \boldsymbol{V}_{i,2} \quad \cdots \quad \boldsymbol{V}_{i,k}], \tag{28}$$

where $\boldsymbol{V}_{i,k}$ are the local reduction bases at k different parameter samples. To ensure orthogonality and avoid numerical instability due to ill-conditioning, a singular value decomposition (SVD) is applied to the independently generated local reduction bases $\boldsymbol{V}_{ip}$. In addition, a threshold on the singular value is set to truncate the left unitary matrix $\boldsymbol{U}$ after SVD to reduce the dimension of this global reduction basis component without significant loss of accuracy. This threshold is defined as $(\sigma_{all}-\sigma_{ts})/\sigma_{all}$, in which σ_{ts} and σ_{all} represent the summation of largest singular values when the threshold is reached and the summation of all singular values, respectively.

Since the improved LCCM also relies on the second order Krylov subspace method, the same approach as for $\boldsymbol{V}_{ip}$ is applied in order to obtain the orthogonal reduction basis $\boldsymbol{V}_{bp}$ for the interface.

6.1.2 Local basis interpolation for $\boldsymbol{\psi}_f$

For the constraint modes $\boldsymbol{\psi}_f$, each column represents a static mode with respect to a unit external load applied to one interface DOF. These interface DOFs all convey the information for the connection of adjacent substructures so that all constraint modes are almost equally important to reflect the interface characteristics. Therefore, the constraint modes can hardly be truncated, otherwise, significant information can be lost. Also, due to the physical meaning of each column dimension, they cannot be column-wise stacked as in the reduction basis for the internal partition. So, to collect the constraint modes from local reduction bases, element-wise interpolation is employed: although this approach is not as accurate as concatenation [39], it avoids strongly increasing the dimension of this global reduction basis component.

For interpolation, the magnitude of the four coefficients $[G_0, G_\infty, \tau, \alpha]$ of the FD model can differ strongly, e.g. α lies between 0 and 1 but G_∞ can differ ten orders of magnitude. Hence, they are first normalized to make their ranges comparable by taking the logarithms $\beta_1=\log_{10}(G_0)/10$, $\beta_2=\log_{10}(G_\infty)/10$, $\beta_3=\log_{10}(\tau)/10$, $\beta_4=\alpha$, and rescaling to the same closed interval [0, 1]. Furthermore, to simplify the interpolation, a new single parameter is defined as the interpolation variable, namely the distance d_m between the vectors $[\beta_1, \beta_2, \beta_3, \beta_4]$ given by:

$$d_m = \left\| [\beta_1, \beta_2, \beta_3, \beta_4]_p - [\beta_1, \beta_2, \beta_3, \beta_4]_m \right\|_2, \tag{29}$$

where m and p represent samples and the targeted parameter set, respectively. Then, the linear interpolation is implemented straightforwardly according to the distances between selected samples and a given targeted parameter set:

$$\boldsymbol{\psi}_{fp} = \sum_m ((1/d_m)\boldsymbol{\psi}_{f,m}) / \sum (1/d_m), \tag{30}$$

where $\boldsymbol{\psi}_{fp}$ and $\boldsymbol{\psi}_{f,m}$ are the constraint modes at the targeted parameter set and selected samples, respectively, and d_m represents the distance between the given parameter set and the mth sample.

6.1.3 Global reduction basis of the substructure

With the different approaches to determine the different global basis components from their corresponding local bases defined, the global reduction basis $\boldsymbol{V}_{gp}$ for the frequency-dependent viscoelastic substructure with varying parameters is obtained as

$$\boldsymbol{V}_{gp} = \begin{bmatrix} \boldsymbol{V}_{ip} & \boldsymbol{\psi}_{fp}\boldsymbol{V}_{bp} \\ \boldsymbol{0} & \boldsymbol{V}_{bp} \end{bmatrix}. \tag{31}$$

Applying this reduction basis to Eq. (7), the pROM of the joint substructure is expressed as

$$(s^2\boldsymbol{M}_r + G(s)\boldsymbol{K}_{vr} + \boldsymbol{K}_{er})\boldsymbol{q}_r = \boldsymbol{F}_r + \boldsymbol{g}_r. \tag{32}$$

In this expression, the benefit of the affine parameter dependency can be observed. Once the pROM of the joint substructure is constructed, only the scalar function related to the frequency-dependency needs to be modified when one wants to change the viscoelastic parameters.

6.2 Reassembly of the system model

The pROM of the viscoelastic substructure is connected to the other substructures for the dynamic analysis of the entire system, based on primal assembly. Since the interiors and interfaces are already divided using the CB method, the information from the global reduction basis can help to build the compatibility relation for each interface of adjacent substructures. For the connection between a reduced joint substructure and a neighboring unreduced, non-joint substructure, it can be expressed as

$$\boldsymbol{q}_{b,\theta}^{(l_i)} = \boldsymbol{V}_{gp,\theta}^{(l_j)} \boldsymbol{q}_{br,\theta}^{(l_j)}, \tag{33}$$

with $\boldsymbol{q}_{br,\theta}^{(l_j)}$ the reduced displacement vector of the θth interface and $\boldsymbol{V}_{gp,\theta}^{(l_j)}$ the reduction basis extracted from $\boldsymbol{V}_{gp}^{(l_j)}$ for the θth interface, in the l_jth substructure that contains viscoelastic materials. $\boldsymbol{q}_{b,\theta}^{(l_i)}$ represents the displacement vector of this interface in the unreduced adjacent substructure.

For the connection between a reduced joint substructure and an adjacent reduced, non-joint substructure, this relation can be formulated as

$$\begin{aligned} \boldsymbol{V}_{\mathrm{CB},\theta}^{(l_i)} \boldsymbol{q}_{br,\theta}^{(l_i)} &= \boldsymbol{V}_{gp,\theta}^{(l_j)} \boldsymbol{q}_{br,\theta}^{(l_j)} \\ \boldsymbol{V}_{\mathrm{CB},\theta}^{(l_i)\,\mathrm{T}} \boldsymbol{V}_{\mathrm{CB},\theta}^{(l_i)} \boldsymbol{q}_{br,\theta}^{(l_i)} &= \boldsymbol{V}_{\mathrm{CB},\theta}^{(l_i)\,\mathrm{T}} \boldsymbol{V}_{gp,\theta}^{(l_j)} \boldsymbol{q}_{br,\theta}^{(l_j)} \\ \boldsymbol{q}_{br,\theta}^{(l_i)} &= (\boldsymbol{V}_{\mathrm{CB},\theta}^{(l_i)\,\mathrm{T}} \boldsymbol{V}_{\mathrm{CB},\theta}^{(l_i)})^{-1} \boldsymbol{V}_{\mathrm{CB},\theta}^{(l_i)\,\mathrm{T}} \boldsymbol{V}_{gp,\theta}^{(l_j)} \boldsymbol{q}_{br,\theta}^{(l_j)} \end{aligned}, \tag{34}$$

where $\boldsymbol{V}_{\mathrm{CB},\theta}^{(l_i)}$ is the reduction basis for the θth interface in the reduced adjacent non-joint substructure. Since both sides in the equation have the reduced dimension on the column, it will always result in the unique exact solution. In this work, the reduced non-joint substructures are generated by the standard CB method and LCCM, since they are considered as regular linear elastic substructures. These relations are used to form the final non-Boolean matrix $\boldsymbol{L}$, in correspondence to Eq. (8), which is then used to reassemble the entire system expressed as

$$(s^2 \boldsymbol{L}^{\mathrm{T}} \boldsymbol{V}_t^{\mathrm{T}} \boldsymbol{M}_t \boldsymbol{V}_t \boldsymbol{L} + G(s) \boldsymbol{L}^{\mathrm{T}} \boldsymbol{V}_t^{\mathrm{T}} \boldsymbol{K}_{vt} \boldsymbol{V}_t \boldsymbol{L} + \boldsymbol{L}^{\mathrm{T}} \boldsymbol{V}_t^{\mathrm{T}} \boldsymbol{K}_{et} \boldsymbol{V}_t \boldsymbol{L}) \boldsymbol{q}_r = \boldsymbol{F}_r, \tag{35}$$

where

$$\begin{aligned} &\boldsymbol{M}_t = \mathrm{diag}(\boldsymbol{M}^{(1)} \quad \boldsymbol{M}^{(2)} \quad \cdots \quad \boldsymbol{M}^{(l)}), \quad \boldsymbol{K}_{vt} = \mathrm{diag}(\boldsymbol{K}_v{}^{(1)} \quad \boldsymbol{K}_v{}^{(2)} \quad \cdots \quad \boldsymbol{K}_v{}^{(l)}), \\ &\boldsymbol{K}_{et} = \mathrm{diag}(\boldsymbol{K}_e{}^{(1)} \quad \boldsymbol{K}_e{}^{(2)} \quad \cdots \quad \boldsymbol{K}_e{}^{(l)}), \quad \boldsymbol{V}_t = \mathrm{diag}(\boldsymbol{V}^{(1)} \quad \boldsymbol{V}^{(2)} \quad \cdots \quad \boldsymbol{V}^{(l)}), \\ &\boldsymbol{q}_r = \boldsymbol{L}^{\mathrm{T}} \boldsymbol{V}_t^{\mathrm{T}} [\boldsymbol{q}^{(1)} \quad \boldsymbol{q}^{(2)} \quad \cdots \quad \boldsymbol{q}^{(l)}]^{\mathrm{T}}, \quad \boldsymbol{F}_r = \boldsymbol{L}^{\mathrm{T}} \boldsymbol{V}_t^{\mathrm{T}} [\boldsymbol{F}^{(1)} \quad \boldsymbol{F}^{(2)} \quad \cdots \quad \boldsymbol{F}^{(l)}]^{\mathrm{T}}. \end{aligned}$$

The reduction basis $\boldsymbol{V}_t$ is the collection of reduction bases $\boldsymbol{V}^{(l)}$ of all substructures, which can be $\boldsymbol{V}_{ap}$ for viscoelastic substructures and $\boldsymbol{V}_{\mathrm{CB}}$ for other substructures. It is noted that $\boldsymbol{V}^{(l)}$ can be also replaced by the identity matrix $\boldsymbol{I}$ for unreduced substructures. The term related to the internal force $\boldsymbol{g}$ in the right side is again eliminated upon applying the $\boldsymbol{L}$ matrix, according to the primal assembly.

With Eq. (35), the original model is solved to the reduced DOFs $\boldsymbol{q}_r$ more efficiently. Using the reduction basis $\boldsymbol{V}_t$, the solution in terms of the unreduced physical DOFs are retrieved by back-projection.

7 Numerical results

In this section, the performance of the developed pMOR method is demonstrated with two numerical examples. In the first example, a simple lap joint is considered to investigate the performance of the improved method for the reduction of the joint substructure, while the other substructures remain unreduced. This example is also used to analyze each improvement separately, to provide more insights into the methodology. The second example considers a larger model of a simplified aircraft wing flap to illustrate the application of the proposed method when the other linear elastic substructures are reduced by the standard CB method. All computations are performed on a laptop with a 2.60 GHz Intel(R) Core(TM) i7-8850H CPU and 16.0 GB RAM. The FE matrices are extracted from Simcenter 3D and pre-processed in Matlab 2020b for pMOR.

The accuracy and computation time reduction are the two main performance indicators. The accuracy is assessed using the average relative error E between the frequency responses $H_n(s)$ computed with the ROM and $H_N(s)$ computed with the FOM, and is expressed as

$$E = \sum (|H_N(s)-H_n(s)|/|H_N(s)|) /Num, \quad (36)$$

with Num the total number of considered frequencies. The time reduction R is defined as:

$$R = (T_{FOM}-T_r)/T_N \times 100\%, \quad (37)$$

with T_{FOM} the computation time of the FOM, and T_r the computation time of the (p)ROM, consisting of the time to solve the (p)ROM and the time needed to perform the back-projection to the unreduced physical DOFs. Additionally, another time reduction R_T is defined by replacing T_r with T_T in Eq. (37) which also includes the time required for generating the ROM.

7.1 Simple lap joint model

7.1.1 Model description

The single-lap joint model consists of two identical 250×50×4 mm^3 aluminum (density 2700 kg/m^3, Young's modulus 67 GPa and Poisson's ratio 0.3) plates connected by a 125×50×5 mm^3 adhesive layer (Figure 3). The bottom plate is clamped at its left end, and a vertical unit force (black arrow) is applied at the right end of the top plate. To construct the pROM later, a common range is considered for the adhesive's viscoelastic material parameters [28] (Table 1), while its density and Poisson's ratio are 1600 kg/m^3 and 0.495, respectively. The structure is discretized using 8-node linear hexahedral elements, resulting in a FOM size of 15048 DOFs after applying boundary conditions. This FE model is divided into three substructures: one viscoelastic adhesive joint substructure and two substructures only containing aluminum. Frequency responses are computed at the free end in the range from 1 Hz to 999 Hz, with a 2 Hz step.

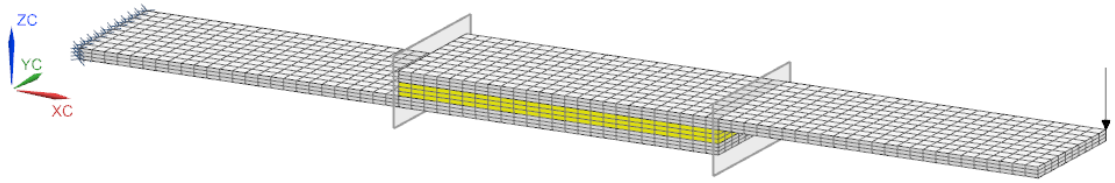

Figure 3: Geometry and FE meshes of the single lap joint model (adhesive layer is highlighted in yellow).

Table 1: Viscoelastic material parameter ranges for the four FD model parameters.

G_0 (Pa)	G_∞ (Pa)	τ (s)	α
$\{10^4, 10^6\}$	$\{10^7, 10^9\}$	$\{10^{-7}, 10^{-5}\}$	{0.6, 0.8}

7.1.2 Performance of the improvements to the CB method and LCCM

For the reference FOM, a fixed set of values is selected for the viscoelastic parameters from the ranges in Table 1: $\{G_0, G_\infty, \tau, \alpha\}$ = {36.56 kPa, 365.6 MPa, 1.226e-6 s, 0.8}. To construct a corresponding ROM, the expansion point is chosen at 900 Hz for the internal and interface reduction, and at 300 Hz for the constraint modes. The orders for the internal reduction and interface reduction are both set as 100. More insights into these selections will be provided later. Finally, the joint substructure model size is reduced from 8580 to 200 DOFs, resulting in a reduction of the assembled model size from 15048 to 6618 DOFs. The frequency responses of the reference FOM and the ROM are compared in Figure 4, showing good agreement with a low average relative error of 7.9e-3. The computation time of the FOM is 423.1 s, while generating and computing the ROM takes 14.0 s and 100.1 s, respectively. This results in an R_T of 73.0%. If only the computation times are compared, the achieved R is 76.3%, indicating that setting up this ROM is relatively fast.

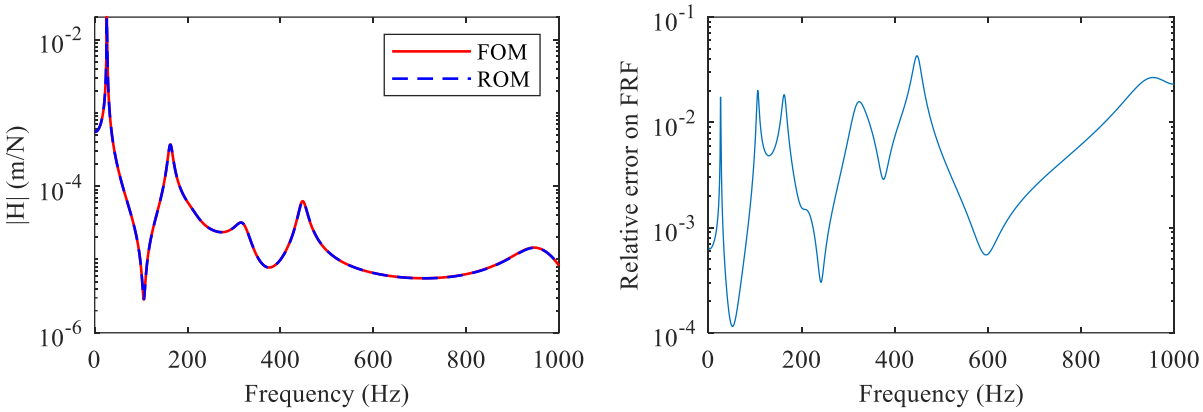

Figure 4: Comparison of frequency responses computed with FOM and ROM (left) and relative error (right).

To gain more insight into the performance of the proposed methodology and the selection of its parameters, the improved CB method and improved LCCM are next investigated separately.

(i) Error from the improved CB method

The reduction basis for the internal partition and the constraint modes are two improvements to the CB method. Therefore, the selection of the expansion points and the order of vectors from the Krylov subspace are investigated, as well as the selection of expansion points for the constraint modes in conjunction with the one for the internal reduction.

First, to analyze the improvement to the reduction basis for the internal partition, different expansion points are investigated (100-900 Hz) in combination with different orders. The expansion point for the frequency-dependent constraint modes is set the same as for the internal reduction. Later it will be selected separately. The error of the ROM with different expansion points and orders is summarized in Figure 5. For each expansion point, increasing the order improves the accuracy, but increases the ROM size and its computational time as well. Conversely, at a fixed order, the expansion point selection has a considerable influence on the accuracy as well, without affecting the ROM size. This is because the frequency-dependency in the model is approximated by the Taylor expansion, so that the used Krylov subspace for generating the reduction basis and frequency-dependent constraint modes are influenced by this expansion point. So by careful selection of the expansion point, low errors can already be achieved for low orders.

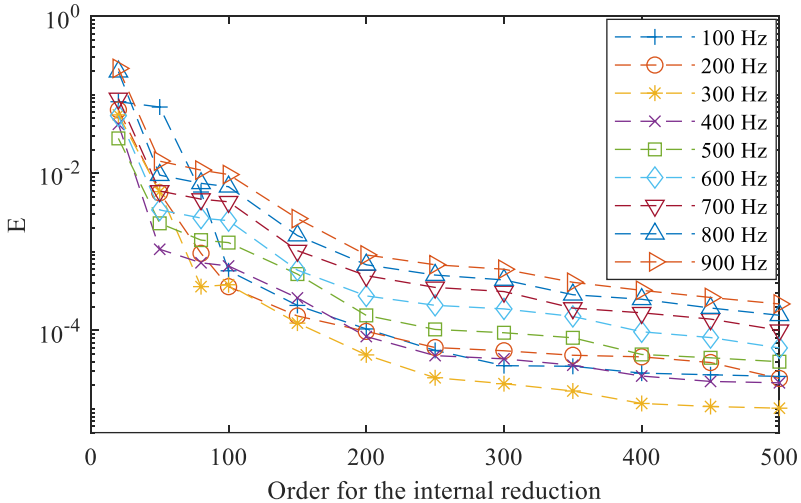

Figure 5: Accuracy of the improved CB method with regard to the order of vectors from the Krylov subspace and the expansion point for the internal reduction, where the expansion point for the constraint modes is selected the same as for the internal reduction; each curve corresponds to different expansion points listed in the legend.

The time reduction in this analysis mainly depends on the order for the internal reduction, which influences the times required for both generating and computing the ROM. This is shown by comparing

R_T and R in Figure 6: both monotonously decrease, with increasing difference when the order increases. The computation time details are listed in Table 2, with T_{CM}, T_{Vi} and T_c the times required for computing the constraint modes, computing the internal reduction basis and for constructing the ROM (including projection and assembly), respectively. Comparing the accuracy and time reduction indicates that the expansion point and order choice allows to make a trade-off according to specific requirements. For instance, if the average relative error has to be lower than 1e-4, an R_T of 65.8% and an R of 73.0% can be achieved according to Figure 5 and Figure 6, respectively.

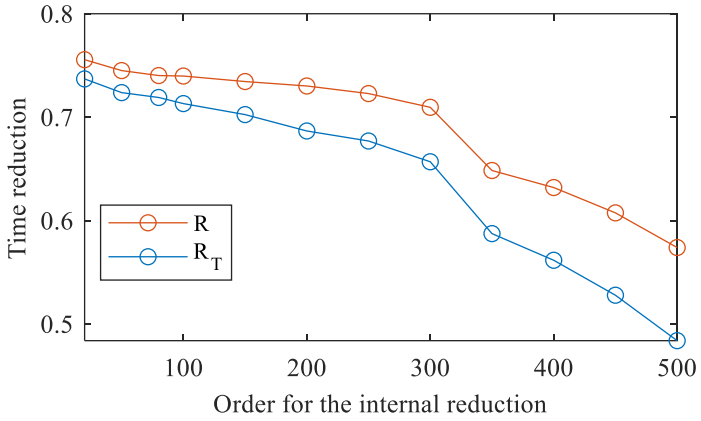

Figure 6: Time reduction of the improved CB method with regard to the order for the internal reduction.

Table 2: Time distribution for generating and computing the ROMs of Figure 6.

Order	20	50	80	100	150	200	250	300	350	400	450	500
T_{Vi} (s)	2.3	3.3	4.5	5.4	7.7	10.2	13.2	16.0	19.4	23.1	26.7	31.1
T_{CM} (s)	4.7	4.7	4.7	4.7	4.7	4.7	4.7	4.7	4.7	4.7	4.7	4.7
T_c (s)	0.9	1.0	1.1	1.2	1.3	1.5	1.5	1.7	1.9	2.0	2.1	2.3
T_r (s)	103.4	107.9	108.6	110.1	112.2	116.2	117.3	122.8	148.6	155.7	166.3	180.3
T_{FOM} (s)	423.1											

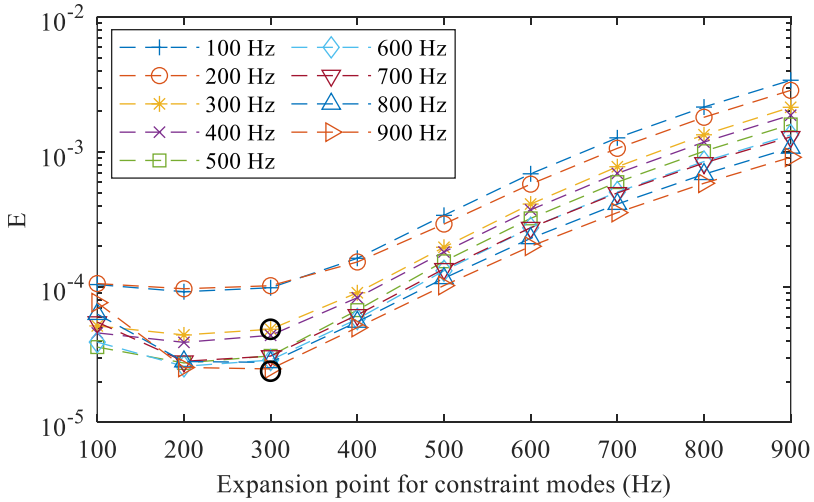

Figure 7: Accuracy of the improved CB method with regard to the expansion points for the internal partition and constraint modes; each curve corresponds to expansion points for the Krylov subspace of the internal partition as listed in the legend; the upper and lower black circles indicate the highest accuracy in Figure 5 and this figure, respectively.

Next, the impact of selecting different expansion points for the reduction basis of the internal partition and the constraint modes is investigated. To this end, the order for the internal reduction is fixed at 200 and the ROM accuracy is evaluated at different expansion point combinations ranging from 100 to 900 Hz (Figure 7). Increasing the constraint modes expansion point shows a similar trend of the error at each internal partition expansion point for this case. As a result, and since the internal reduction and

constraint modes are linearly combined, the influence from both expansion points can be regarded as independent. By selecting different instead of the same expansion points for these two bases, significant accuracy gains can be achieved (indicated by the black circles in Figure 7). Consequently, selecting expansion points for the internal reduction and constraint modes separately can help to generate more accurate ROMs without increasing the order. In this case, the smallest error occurs when 900 Hz and 300 Hz are selected for the internal reduction and constraint modes, respectively. Hence, these are continued with in what follows.

(ii) Error from the improved LCCM

To assess the accuracy of the improved LCCM, four different orders are used to construct the corresponding ROMs. For all cases, the expansion points for the internal partition and the constraint modes are fixed as 900 Hz and 300 Hz as investigated before, and the expansion point for the improved LCCM is set as 900 Hz. Then, the order for the internal reduction is increased for all the ROMs with LCCM, and the errors are compared (Figure 8).

As opposed to Figure 5, where increasing the internal reduction order strongly affects the accuracy if only internal reduction is applied (black reference curve in Figure 8), the interface reduction now appears as the main restriction in terms of accuracy: even for relatively low internal reduction orders, the accuracy quickly stagnates at a level which is governed by the interface reduction order and becomes insensitive to further increasing the internal reduction order. This is because LIR is less accurate compared to the internal reduction with preserved interface DOFs, since mass and stiffness contributions of neighboring substructures are not accounted for when setting up the ROM [40]. Hence, when performing internal and interface reduction, since the accuracy is primarily governed by the interface reduction order, the internal reduction order can be kept relatively low without further affecting the overall accuracy much while still providing usable accuracy levels below 10^{-2}.

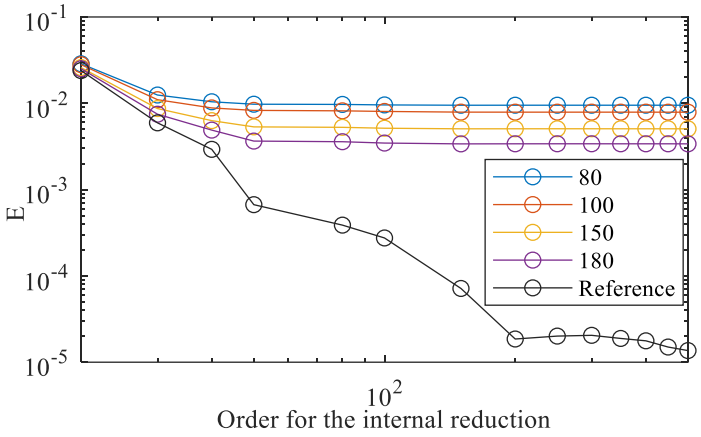

Figure 8: Accuracy of the ROMs with the improved LCCM for different orders for the internal reduction, whereby the expansion point of the LCCM is fixed at 900 Hz; the reference curve has the same settings as other curves but without the LCCM; the legend indicates the order for the improved LCCM.

Next, the influence of the expansion point and order of the improved LCCM on the accuracy is investigated in more detail. To this end, the expansion point and order for the internal reduction are fixed at 900 Hz and 100 respectively, the expansion point for the constraint modes is fixed at 300 Hz, while the interface reduction order is varied from 20 to 150 at different interface expansion points between 100 and 900 Hz (Figure 9). The ROM error decreases with increasing order of the improved LCCM regardless of the expansion point (Figure 9, left). Since the error for each order of the improved LCCM is almost constant with regard to the expansion point (Figure 9, right), except for the lowest order which overall leads to inaccurate results, the influence of the expansion point for the interface is weaker than for the internal reduction as observed in Figure 5.

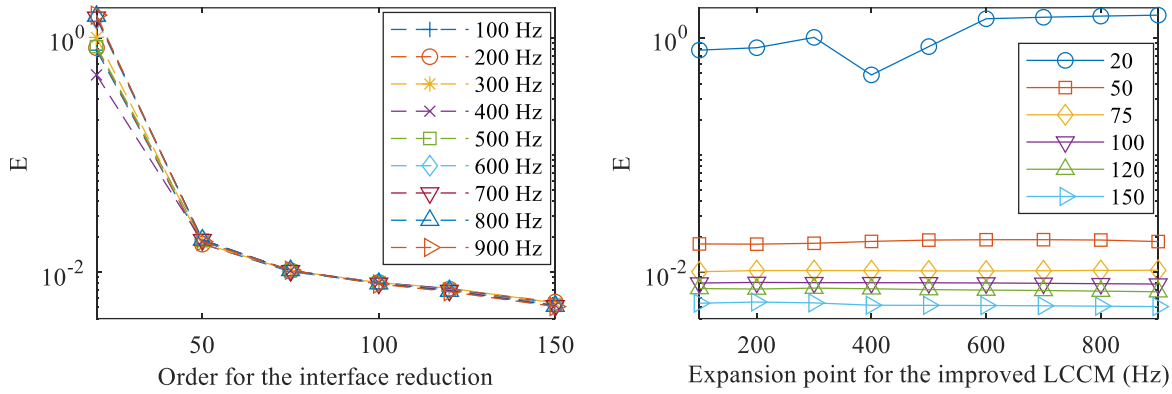

Figure 9: Accuracy of the improved CB method with LIR with regard to the order (left) and the expansion point of LCCM (right), with the expansion point for the constraint modes fixed at 300 Hz, and the expansion point and order for the internal reduction are fixed as 900 Hz and 200; values in the left legend represent different expansion points for the improved LCCM, and values in the right legend represent different orders of the improved LCCM.

The time reduction of the ROM with and without LCCM is compared for the same internal reduction order of 100 (Figure 10). The detailed computation time contributions for the ROM with and without LCCM are listed in Table 3, where the time required for constructing the improved LCCM T_{Vb} has been added. It is obvious that applying LCCM helps to gain more time reduction in both R and R_T. Meanwhile, with the increased order for the interface reduction, less time reduction is gained. Additionally, R_T for the ROM with LCCM approaches to the case without LCCM faster than R mainly due to the increase both in T_{Vb} and T_r. Combined with Figure 9 to both evaluate the accuracy and time reduction, the trade-off can be made as well. The significance and effects of LCCM on time reduction will be further shown in the next case in Section 7.2.

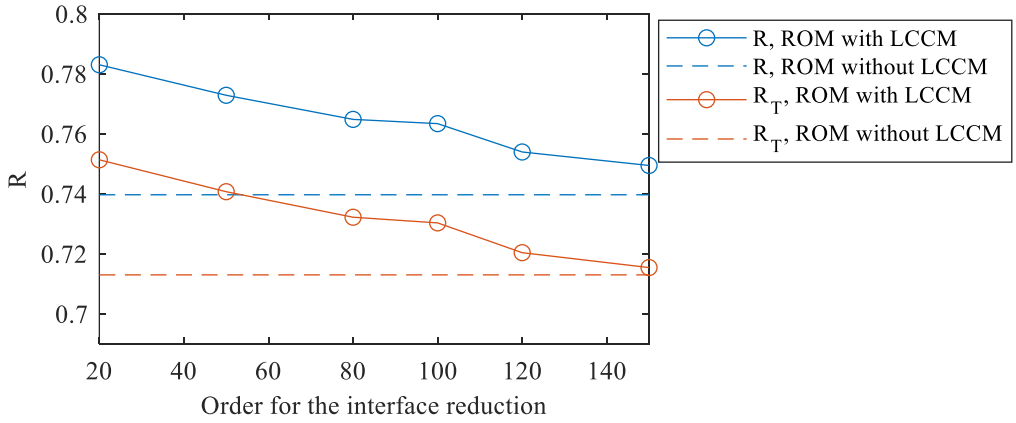

Figure 10: Time reduction of the ROM with LCCM with regard to the order for the interface reduction.

Table 3: Time distribution for generating and computing the ROM with and without LCCM.

Order	20	50	80	100	120	150	without
T_{Vi} (s)	5.4	5.4	5.4	5.4	5.4	5.4	5.4
T_{CM} (s)	4.7	4.7	4.7	4.7	4.7	4.7	4.7
T_{Vb} (s)	2.4	2.6	2.7	2.9	3.0	3.1	/
T_c (s)	0.9	0.9	1.0	1.0	1.1	1.2	1.2
T_r (s)	91.8	96.1	99.5	100.1	104.1	106.0	110.1

7.1.3 pMOR strategy

In this section, the performance of the proposed pMOR approach is investigated. The four FD model parameters $\{G_0, G_\infty, \tau, \alpha\}$ are considered as the parameters of the viscoelastic joint substructure pROM. To generate a low number of samples in the parameter space (Table 1) to construct the pROM, the low-discrepancy Sobol sequence is employed. By following the procedure in [28], four samples are selected

(Table 4) to construct the global reduction basis. The scrambled Sobol points are obtained by the built-in Matlab functions *sobolset* and s*cramble*.

Table 4: Four samples computed from the Sobol points.

	G_0 (Pa)	G_∞ (Pa)	τ (s)	α
Sample 1	1.1455e4	1.3970e8	1.3964e-6	0.7483
Sample 2	5.4576e5	8.9289e7	2.0258e-7	0.6940
Sample 3	4.4463e4	1.7840e7	8.0686e-6	0.6038
Sample 4	1.2224e5	3.8619e8	3.2704e-7	0.7511

The same settings for constructing the ROM in the previous subsection are retained to construct the pROM. Setting the SVD thresholds for the internal and interface reduction as 1e-5 and 1e-4, respectively, results in a pROM size of 443 DOFs for the joint substructure. Due to the global basis, this is larger than the joint substructure ROM introduced in the beginning of Section 7.1.2 for one set of parameter values, which was 200 DOFs. The pROM accuracy is first evaluated at the same parameter values {36.56 kPa, 365.6 MPa, 1.226e-6 s, 0.8} used for constructing the FOM and ROM in Section 7.1.2, and which were not included in the pROM construction. As shown in Figure 11, this pROM approximates the FOM well, with an average relative error of 3.7e-3. Moreover, the pROM leads to a lower error than the ROM, which has an average relative error of 7.9e-3. This can be explained by the larger pROM containing more information from different samples, which helps to improve its accuracy.

The time for generating and computing this pROM are 65.7 s and 114.2 s, respectively, resulting in an R of 73.0% and R_T of 57.5%. Compared to the ROM, with R of 76.3% and R_T of 73.0%, the pROM for this single evaluation leads to a slightly lower computation time reduction, which becomes considerably lower when the pROM construction is also considered. However, in case results for a range of different parameter values need to be computed, the pROM can simply be evaluated for these parameter values, whereas the ROM needs to be completely re-constructed. Contrarily, re-evaluating the pROM for a different set of parameter values only requires changing the values of the scalar function as the coefficients of the complex stiffness matrix, and costs almost no extra time. Hence, in those cases, the only once spent pROM construction time can eventually be neglected and the R of the pROM should instead be compared to the R_T of the ROM, showing that the pROM enables the same time reduction, yet in this case also higher accuracy. A ROM of the same accuracy in this case needs the reduced dimension of 275 DOFs, resulting in an R_T of 69.9% (generating and computing this new ROM costs 127.3 s). This is lower than the R of 73.0% of the pROM. Therefore, it is worthwhile to construct the pROM to achieve extra time reduction while preserving accuracy, in particular when many computations for different parameters are required.

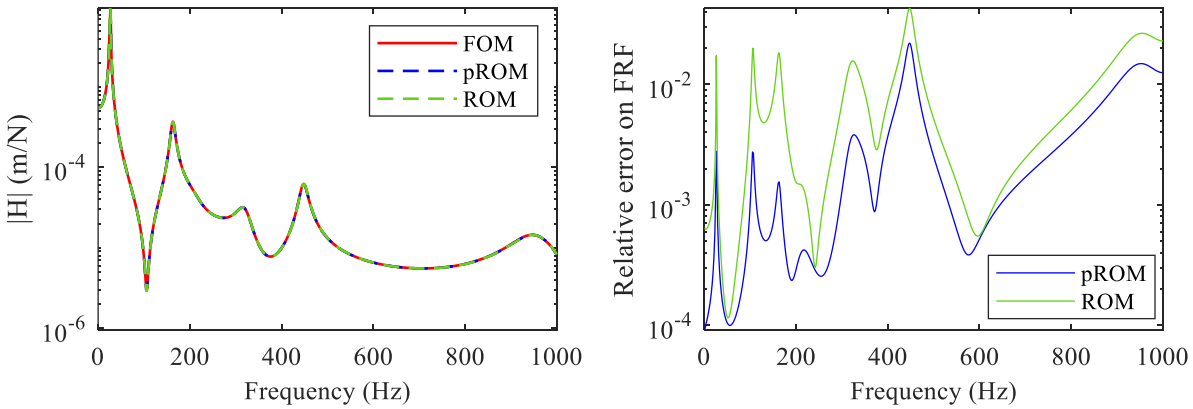

Figure 11: Comparison of frequency responses computed with the FOM and the pROM.

To investigate the error distribution across the parameter space, four evenly distributed points are selected for each parameter and the average relative error of the corresponding FRFs for each parameter combination is computed (Figure 12). The error in this parameter space lies between 2.2e-3 and 9.1e-3 with most cases below 5e-3, which is a relatively small variation. The worst case occurs at parameter set {3.4e5 Pa, 1e7 Pa, 1e-7 s, 0.8} for {G_0, G_∞, τ, α}. The average error with regard to the normalized

average distance to the four samples for all the test parameter sets are present in Figure 13. With increasing distance, in general larger errors can occur, although still overall accurate results can be obtained with the pROM.

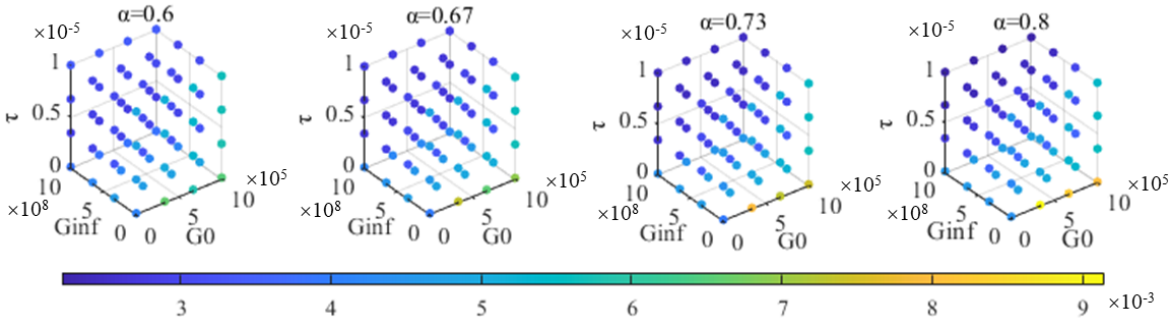

Figure 12: Error distribution in the four-dimensional parameter space through test points.

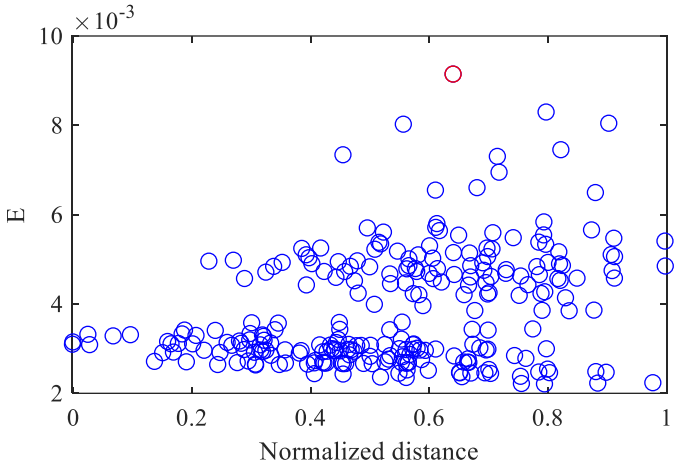

Figure 13: Error distribution with regard to the average distance to the sampling points; the red point represents the largest error.

The accuracy of the global reduction basis also depends on the SVD truncation threshold for the construction of the global reduction basis. To assess this, the influence of the SVD threshold for the internal reduction is investigated, while keeping the SVD threshold for the interface fixed at 1e-4. The pROM is evaluated for parameters {3.4e5 Pa, 1e7 Pa, 1e-7 s, 0.8}, the set with the largest error in all tested parameter sets, and the influence of the local reduction bases size and the SVD threshold on the accuracy is shown (Figure 14). Each curve corresponds to a specific dimension of the sampled local reduction bases expressed in terms of the internal reduction order, and shows the average relative error versus the dimension of the internal partition after pMOR. This dimension is governed by the SVD threshold for the internal reduction, with a smaller threshold leading to an increased internal partition dimension. Comparing the three curves, it is evident that increasing the dimension of the sampled local reduction bases does not always significantly improve the accuracy as opposed to applying a lower SVD threshold. For instance, at dimension 306 of the internal reduction in the global reduction basis (dashed line in Figure 14) the smallest error is obtained when the order for the internal reduction in the local reduction bases is 100 and the SVD threshold is 1e-6. For the other two curves, smaller thresholds have to be used to obtain the same accuracy, which leads to larger dimensions of the pMOR. This illustrates the trade-off between the local reduction basis dimension and SVD thresholds. Therefore, it might be more favorable to choose a relatively low local basis dimension, but in combination with a lower SVD threshold, as this might produce an equally large yet more accurate pROM. Moreover, as evident from the computation time comparisons in Figure 15, such a strategy would also allow obtaining a greater computation time reduction.

Besides the SVD threshold and local reduction bases dimensions, the number of samples could also have an influence on this balance. However, a detailed investigation of the advantage and influence of different quasi-random sampling strategies is out of scope of this work.

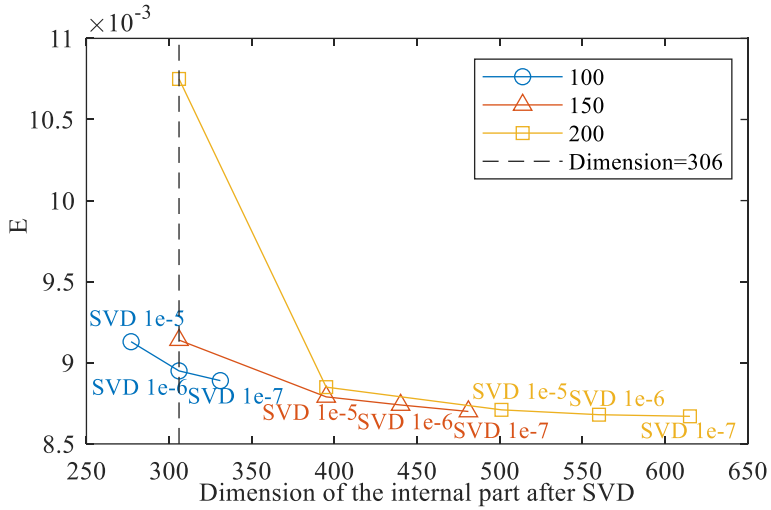

Figure 14: Accuracy of pROM with regard to the order for the internal reduction in the global reduction basis; 100, 150, and 200 in the legend indicate the order for the internal reduction in the local reduction bases

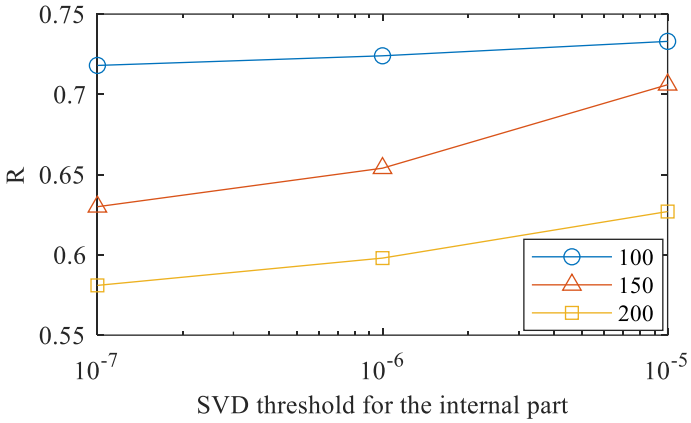

Figure 15: Time reduction with regard to the SVD threshold for the internal reduction, 100, 150, and 200 in the legend indicate the order for the internal reduction in local reduction bases

This example demonstrates that the proposed pMOR method which includes the improved CB and LCCM to incorporate viscoelastic frequency-dependency can be successfully applied to adhesive joint substructures. Although no additional reduction of the other substructures was considered so far, the methodology already enables reducing the viscoelastic substructure with good accuracy and considerable time reduction.

7.2 Application to a simplified wing flap model

In this second example, the proposed pMOR methodology for substructures containing viscoelasticity is combined with the conventional MOR for the reduction of the remaining linear elastic substructures in the system. This enables improving the computational efficiency of large system assemblies with viscoelastic adhesive joints, and in general also localized viscoelastic material additions, while maintaining good accuracy and providing compatibility with local parameter changes of the viscoelastic material properties.

7.2.1 Model description

A section of a simplified wing flap model is considered, which contains two aluminum components that are connected by two adhesive layers (Figure 16). The aluminum and viscoelastic adhesive material both have the same properties as in previous example. This structure is decomposed into six substructures according to the location of two adhesive joints, indicated by different colors (joints in green). The entire structure is modelled using linear hexahedral elements, which results in a total of 153114 DOFs. The number of DOFs of each substructure are listed in Table 5. The boundary conditions

are simplified as fixed constraints at the top, indicated in dark blue in Figure 16, and a horizontal unit point force excitation is applied along the positive direction of the *xc* axis, indicated by the red arrow. Frequency responses are computed in the range from 1 Hz to 999 Hz, with a 2 Hz step.

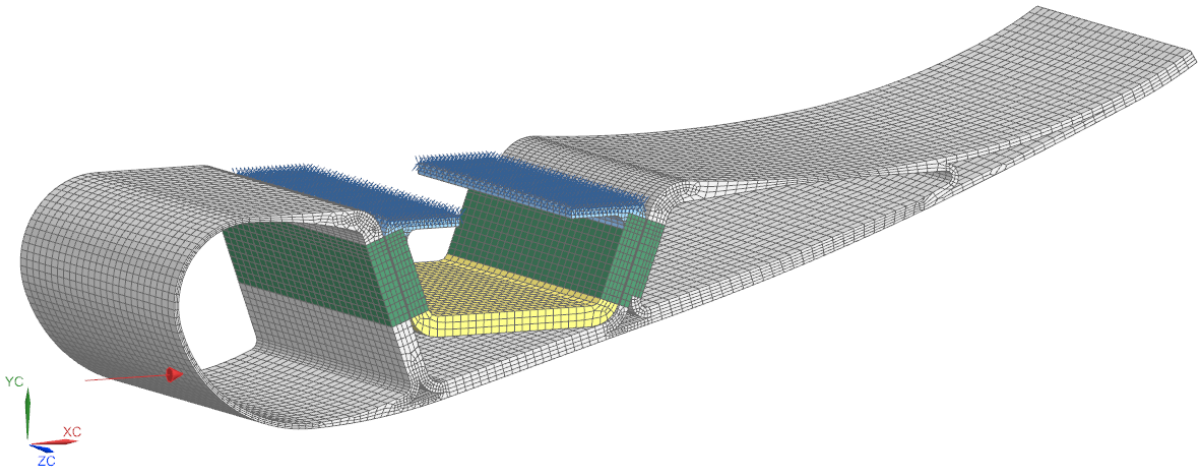

Figure 16: Geometry and mesh distribution; fixed constraints at the top and a horizontal unit point force excitation from left side.

Table 5: Composition and reduction of the flap model.

	Internal DOFs						Interface DOFs	
	Green (left)	Green (right)	Blue (left)	Blue (right)	Yellow	Gray	Green (left)	Green (right)
FOM	15210	15912	5772	5460	9024	105846	2028	2262
ROM	150	150	150	150	150	600	400	400
pROM	353	358	150	150	150	600	1072	1072

7.2.2 pMOR application

To demonstrate the improved efficiency of the proposed pMOR method, the joint substructures and the other substructures are now all reduced. This will also illustrate the successful assembly of the adhesive joint substructure pROMs with other substructures reduced by the standard CB with LCCM.

For the reduction of the viscoelastic joint substructures, several parameters need to be chosen. Since the same viscoelastic material and the same parameter ranges including frequency are used, the same expansion points, 900 Hz for the internal and interface reduction and 300 Hz for constraint modes, are selected as investigated in the preceding case. However, the selection of orders for the internal and interfaces should be based on the model size. According to the analysis of Figure 8, the LCCM is the main bottleneck of the error. For this case, to construct local reduction bases, the order for the internal reduction is taken as a relatively small number 150, and a relatively larger number 400, is chosen for the order of the improved LCCM. For the extension to the pROM, since the viscoelastic parameter ranges are kept the same, the same four samples as in the previous numerical example are used. Also, thresholds 1e-5 and 1e-4 are used for the internal reduction and interface reduction, respectively. The reduced order model sizes of all substructures are listed in Table 5. To assess the performance of the pROM, the FOM is constructed using again the same parameter set $\{G_0, G_\infty, \tau, \alpha\}$ = {36.56 kPa, 365.6 GPa, 1.226e-6 s, 0.8} as before. To compare with the pROM, both a ROM with and without LCCM are also constructed, with the reduced dimensions listed in Table 5. In case of the pROM for the adhesive substructure, the concatenation of local bases and subsequent truncation after SVD leads to a larger model size as compared to the ROM. However, the pROM is again constructed to be valid over a wide parameter range, whereas the ROMs are not. The construction and computation time for these models are listed in Table 6, and the comparison in terms of FRFs and errors is shown in Figure 17.

The ROM without LCCM well approximates the FOM, with the E of 1.2e-3 and R of 90.3%. After applying the LCCM, the achieved error E increases to 1.6e-2, which is still an acceptable accuracy. However, the LCCM results in a smaller model size and an R of 99.1%, which leads to an 11.2 times faster computation than the ROM without LCCM. When also accounting for the higher basis

computation and the construction (projection and assembly) time, the ROM with LCCM is still about 1.8 times faster, with an R_T of 90.2% as compared to 82.8%. The higher construction time for the ROM with LCCM arises from the fact that the submatrices in matrix $\boldsymbol{L}$ in Eq. (35) corresponding to the interface are dense matrices, which require more operations in matrix manipulation compared to the sparse diagonal submatrices in $\boldsymbol{L}$ for the ROM without LCCM despite its larger size. It is obvious that more time reduction is achieved after applying the LCCM in this case as compared to the first case of section 7.1 since more interface DOFs are involved and reduced in the considered joints of the wing-flap model.

Also the pROM approximates the FOM well. The average relative error is 6.7e-3, which is lower than the average error 1.6e-2 of the ROM with LCCM. This is again attributed to the enrichment the different sampled local bases bring to the global pROM basis. Moreover, comparing the achievable time reduction, also here the advantage over the ROM with LCCM of only having to generate the pROM once if different parameter values are to be evaluated, should be taken into account. Although generating the pROM takes 20.2% of T_{FOM} for this case, this timing can again be neglected when the pROM is used for simulations with many different parameter values, such as optimization problems or identification. Hence, the achieved R of 95.5% is higher than the time reduction obtained by the ROM with LCCM, which needs to be re-generated for different parameter values, and is hence given by the R_T of 90.2%. Comparing the T_r = 535.1 s of the pROM with the T_T = 1165.2 s of the ROM with LCCM, this effectively comes down to a speed-up by a factor 2.2. For even larger models, although even more time can be required for the pROM generation, more time reduction can also be achieved with a similar level on dimension reduction, since the time complexity for solving the reduced model is approximately cubic in the reduced model dimension.

This example demonstrates the good performance of the proposed adaptations in terms of time reduction, accuracy, and successful assembly with other substructures reduced by the standard CB method.

Table 6: Time distribution for the reduced models.

Time	ROM without LCCM	ROM with LCCM	pROM	FOM
Reduction basis	820.0 s	980.3 s	1795.7 s	/
Construction	66.8 s	81.4 s	607.8 s	/
Computation	1158.0 s	103.5 s	535.1 s	11900.5 s
R	90.3%	99.1%	95.5%	/
R_T	82.8%	90.2%	75.3%	/

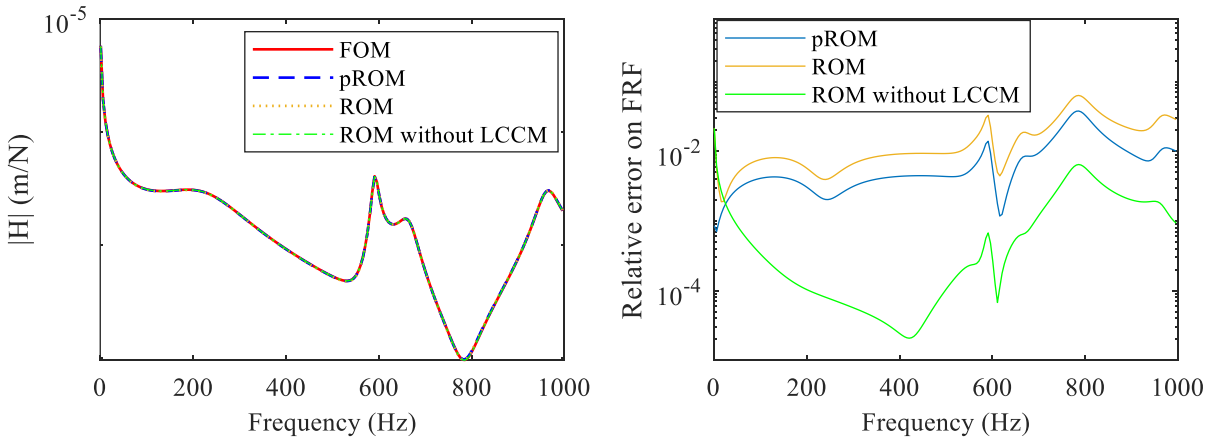

Figure 17: Comparison of frequency responses computed from FOM, ROM and pROM.

8 Conclusions

pMOR combined with substructuring forms a powerful technique to greatly improve the efficiency of analyzing the dynamic performance of large-scale mechanical systems with local property changes. However, no adequate pMOR method existed to directly reduce substructures with frequency-

dependent viscoelastic material properties, often encountered in increasingly applied adhesive bonded assemblies or structures with add-on viscoelastic patches.

To overcome this, this work proposes a pMOR strategy for substructures containing viscoelasticity. To achieve this, four improvements based on the CB method and LCCM have been made: (i) the normal modes for the internal reduction of the conventional CB method are replaced by a reduction basis suitable for frequency-dependency, employing the second order Krylov subspace, generated from the reformulated model after Taylor expansion; (ii) the frequency-dependent constraint modes are transferred to constant counterparts based on the reformulated model after Taylor expansion; (iii) the normal modes used in conventional LCCM are replaced by a reduction basis generated from the second order Krylov subspace to achieve more time reduction for models with large interfaces, and the primal assembly is adapted accordingly; (iv) to make the reduced model compatible with viscoelastic material parameter changes, the improved CB method with LCCM is extended to pMOR by constructing a sampling-based global reduction basis: the internal and the interfaces are constructed by concatenation and orthogonalization, while the constraint modes are constructed by a new way of interpolation.

The proposed (p)MOR methodology has been applied to two models. In both cases, good performance was demonstrated in terms of accuracy and computation time reduction. The results also indicate that the influences from the expansion points of the internal partition and constraint modes on the ROM accuracy are independent and are better selected separately. The LCCM is found to be the main bottleneck for the accuracy of the reduced model, which hence allows to select a relatively small order for the internal reduction to generate a smaller reduced model with LCCM, without significantly lowering the accuracy. The accuracy of the improved LCCM is relatively less sensitive to the selection of the expansion point, compared to the expansion point for the internal partition. The order of local reduction bases and the SVD threshold should both be considered for the balance between the accuracy and the reduction level.

The proposed methodology not only enables the efficient analysis of adhesive bonded assemblies for a variety of viscoelastic material parameters, but can be used to accelerate the structural dynamic analysis of a wide range of structures which also include localized materials containing frequency-dependency such as damping layers or porous materials.

Acknowledgement

This research was partially supported by Flanders Make, the strategic research center for the manufacturing industry. This research is a JOINTTOOL related work. The Research Fund KU Leuven is gratefully acknowledged for its support. The research of L. Van Belle (fellowship no. 1271621N) is funded by a grant from the Research Foundation–Flanders (FWO).

Reference

[1] X. Shang, E. A. S. Marques, J. J. M. Machado, R. J. C. Carbas, D. Jiang, L. F. M. da Silva, Review on techniques to improve the strength of adhesive joints with composite adherends, Compos. Part B Eng. 177 (2019) 107363. 10.1016/j.compositesb.2019.107363.

[2] W. Sun, Z. Wang, X. Yan, M. Zhu, Inverse identification of the frequency-dependent mechanical parameters of viscoelastic materials based on the measured FRFs, Mech. Syst. Signal Process. 98 (2018) 816–833. 10.1016/j.ymssp.2017.05.031.

[3] D. J. McTavish, P. C. Hughes, Modeling of linear viscoelastic space structures, J. Vib. Acoust. Trans. ASME 115 (1) (1993) 103–110. 10.1115/1.2930302.

[4] S. W. Park, Analytical modeling of viscoelastic dampers for structural and vibration control, Int. J. Solids Struct. 38 (44–45) (2001) 8065–8092. 10.1016/S0020-7683(01)00026-9.

[5] M. Sasso, G. Palmieri, and D. Amodio, Application of fractional derivative models in linear viscoelastic problems, Mech. Time-Dependent Mater. 15 (4) (2011) 367–387. 10.1007/s11043-011-9153-x.

[6] K. R. Karim, G. D. Chen, Surface damping effect of anchored constrained viscoelastic layers on the flexural response of simply supported structures, Mech. Syst. Signal Process. 27 (1) (2012) 419–432. 10.1016/j.ymssp.2011.09.006.

[7] S. Valvano, C. Orlando, A. Alaimo, Design of a noise reduction passive control system based

on viscoelastic multilayered plate using P_DSO, Mech. Syst. Signal Process. 123 (2019) 153–173. doi: 10.1016/j.ymssp.2019.01.011.
[8] F. Marchione, Stress distribution in double-lap adhesive joints: Effect of adherend reinforcement layer, Int. J. Adhes. Adhes. 105 (November) (2020) 102780. 10.1016/j.ijadhadh.2020.102780.
[9] C. D. Johnson, D. A. Kienholz, Finite element prediction of damping in structures with constrained viscoelastic layers, AIAA J. 20 (9) (1982) 1284–1290. 10.2514/3.51190.
[10] L. Rouleau, J. F. Deü, A. Legay, A comparison of model reduction techniques based on modal projection for structures with frequency-dependent damping, Mech. Syst. Signal Process. 90 (2017) 110–125. 10.1016/j.ymssp.2016.12.013.
[11] S. Zghal, M. L. Bouazizi, N. Bouhaddi, R. Nasri, Model reduction methods for viscoelastic sandwich structures in frequency and time domains, Finite Elem. Anal. Des. 93 (C) (2015) 12–29. 10.1016/j.finel.2014.08.003.
[12] X. Xie, H. Zheng, S. Jonckheere, A. van de Walle, B. Pluymers, W. Desmet, Adaptive model reduction technique for large-scale dynamical systems with frequency-dependent damping, Comput. Methods Appl. Mech. Eng. 332 (2018) 363–381. 10.1016/j.cma.2017.12.023.
[13] J. C. Trigeassou, T. Poinot, J. Lin, A. Oustaloup, F. Levron, Modeling and identification of a non integer order system, in: 1999 European control conference, 1999, pp. 2453–2458.
[14] K. J. Latawiec, M. Lukaniszyn, R. Stanislawski, Advances in Modelling and Control of Non-integer Order Systems, First ed., Springer, Opole, 2014.
[15] Y. Nakatsukasa, O. Sète, L. N. Trefethen, The AAA algorithm for rational approximation, SIAM J. Sci. Comput. 40 (3) (2018) A1494–A1522. 10.1137/16M1106122.
[16] Z. Bai, Y. Su, Dimension reduction of large-scale second-order dynamical systems via a second-order arnoldi method, SIAM J. Sci. Comput. 26 (5) (2005) 1692–1709. 10.1137/040605552.
[17] Y. Lin, L. Bao, Y. Wei, Model-order reduction of large-scale kth-order linear dynamical systems via a kth-order Arnoldi method, Int. J. Comput. Math. 87 (2) (2010) 435–453. 10.1080/00207160802130164.
[18] Q. Aumann, E. Deckers, S. Jonckheere, W. Desmet, G. Müller, Automatic model order reduction for systems with frequency-dependent material properties, Comput. Methods Appl. Mech. Eng. 397 (2022) 115076. 10.1016/j.cma.2022.115076.
[19] T. Tao, G. Zhao, J. Zhai, S. Ren, A strong adaptive piecewise model order reduction method for large-scale dynamical systems with viscoelastic damping, Mech. Syst. Signal Process. 164 (July) (2021) 108203. 10.1016/j.ymssp.2021.108203.
[20] S. Gugercin, A. C. Antoulas, C. Beattie, H_2 model reduction for large-scale linear dynamical systems, SIAM J. Matrix Anal. Appl. 30 (2) (2008) 609–638. 10.1137/060666123.
[21] K. Sinani, S. Gugercin, C. Beattie, A Structure-preserving Model Reduction Algorithm for Dynamical Systems with Nonlinear Frequency Dependence, IFAC-PapersOnLine, 49 (9) (2016) 56–61. 10.1016/j.ifacol.2016.07.492.
[22] P. Benner, S. Gugercin, K. Willcox, A survey of projection-based model reduction methods for parametric dynamical systems, SIAM Rev. 57 (4) (2015) 483–531. 10.1137/130932715.
[23] B. Fröhlich, D. Hose, O. Dieterich, M. Hanss, P. Eberhard, Uncertainty quantification of large-scale dynamical systems using parametric model order reduction, Mech. Syst. Signal Process. 171 (January) (2022) 108855. 10.1016/j.ymssp.2022.108855.
[24] U. Baur, C. Beattie, P. Benner, Mapping parameters across system boundaries: parameterized model reduction with low rank variability in dynamics, Pamm, 14 (1) (2014) 19–22. 10.1002/pamm.201410006.
[25] S. van Ophem, E. Deckers, W. Desmet, Parametric model order reduction without a priori sampling for low rank changes in vibro-acoustic systems, Mech. Syst. Signal Process. 130 (2019) 597–609. 10.1016/j.ymssp.2019.05.035.
[26] B. N. Bond, L. Daniel, A piecewise-linear moment matching Approach to parameterized model order reduction for highly nonlinear systems, IEEE Trans. Comput. Des. Integr. Circuits Syst. 26 (12) (2007) 2116–2129. 10.1109/TCAD.2007.907258.
[27] T. Soll, R. Pulch, Sample selection based on sensitivity analysis in parameterized model order reduction, J. Comput. Appl. Math. 316 (2017) 369–379. 10.1016/j.cam.2016.09.046.
[28] X. Xie, H. Zheng, S. Jonckheere, B. Pluymers, W. Desmet, A parametric model order reduction technique for inverse viscoelastic material identification, Comput. Struct. 212 (2019) 188–198.

10.1016/j.compstruc.2018.10.013.
[29] H. Panzer, J. Mohring, R. Eid, B. Lohmann, Parametrische ordnungsreduktion mittels matrixinterpolation, At-Automatisierungstechnik 58 (8) (2010) 475–484. 10.1524/auto.2010.0863.
[30] D. De Klerk, D. J. Rixen, S. N. Voormeeren, General framework for dynamic substructuring: History, review, and classification of techniques, AIAA J. 46 (5) (2008) 1169–1181. 10.2514/1.33274.
[31] S. N. Voormeeren, D. J. Rixen, A family of substructure decoupling techniques based on a dual assembly approach, Mech. Syst. Signal Process. 27 (1) (2012) 379–396. 10.1016/j.ymssp.2011.07.028.
[32] R. Craig, M. Bampton, Coupling of Substructures for Dynamic Analyses, AIAA J. 6 (7) (1968) 1313–1319.
[33] R. Macneal, A hybrid method of component mode synthesis, Comput. Struct. 1 (4) (1971) 581–601.
[34] S. Rubin, Improved component-mode representation for structural dynamic analysis, AIAA J. 13 (8) (1975) 995–1006. 10.2514/3.60497.
[35] G. Battiato, C. M. Firrone, T. M. Berruti, B. I. Epureanu, Reduction and coupling of substructures via Gram–Schmidt Interface modes, Comput. Methods Appl. Mech. Eng. 336 (2018) 187–212. 10.1016/j.cma.2018.03.001.
[36] P. Holzwarth, P. Eberhard, Interface reduction for CMS methods and alternative model order reduction, IFAC-PapersOnLine 28 (1) (2015) 254–259. 10.1016/j.ifacol.2015.05.005.
[37] L. Carassale, M. Maurici, Interface Reduction in Craig-Bampton Component Mode Synthesis by Orthogonal Polynomial Series, J. Eng. Gas Turbines Power 140 (5) (2018) 1–8. 10.1115/1.4038154.
[38] M. Castanier, Y. Tan, C. Pierre, Characteristic Constraint Modes for Component Mode Synthesis, AIAA J. (2001) 0–6.
[39] S. K. Hong, B. I. Epureanu, M. P. Castanier, Next-generation parametric reduced-order models, Mech. Syst. Signal Process. 37 (1–2) (2013) 403–421. 10.1016/j.ymssp.2012.12.012.
[40] D. Krattiger, L. Wu, M. Zacharczuk, M. Buck, R. J. Kuether, M. S. Allen, P. Tiso, M. R. W. Brake, Interface reduction for Hurty/Craig-Bampton substructured models: Review and improvements, Mech. Syst. Signal Process. 114 (2019) 579–603. 10.1016/j.ymssp.2018.05.031.
[41] P. Holzwarth, P. Eberhard, SVD-based improvements for component mode synthesis in elastic multibody systems, Eur. J. Mech. A/Solids 49 (2015) 408–418. 10.1016/j.euromechsol.2014.08.009.
[42] S. Van Ophem, E. Deckers, W. Desmet, Efficient assembly of unit cells with Krylov based model order reduction, in: Proc. ISMA 2018 - Int. Conf. Noise Vib. Eng. USD 2018 - Int. Conf. Uncertain. Struct. Dyn., 2018, pp. 445–456.
[43] S. Burgard, O. Farle, D. Klis, R. Dyczij-Edlinger, Order-reduction of fields-level models with affine and non-affine parameters by interpolation of subspaces, IFAC-PapersOnLine 28 (1) (2015) 170–175. 10.1016/j.ifacol.2015.05.111.
[44] O. C. Zienkiewicz, R. L. Taylor, J. Z. Zhu, The Finite Element Method: Its Basis and Fundamentals, Sixth ed., Elsevier, Oxford, 2005.